



AMERICAN METEOROLOGICAL SOCIETY

Journal of Climate

EARLY ONLINE RELEASE

This is a preliminary PDF of the author-produced manuscript that has been peer-reviewed and accepted for publication. Since it is being posted so soon after acceptance, it has not yet been copyedited, formatted, or processed by AMS Publications. This preliminary version of the manuscript may be downloaded, distributed, and cited, but please be aware that there will be visual differences and possibly some content differences between this version and the final published version.

The DOI for this manuscript is doi: 10.1175/JCLI-D-13-00173.1

The final published version of this manuscript will replace the preliminary version at the above DOI once it is available.

If you would like to cite this EOR in a separate work, please use the following full citation:

Smith, K., M. Previdi, and L. Polvani, 2013: The Antarctic Atmospheric Energy Budget. Part II: The Effect of Ozone Depletion and its Projected Recovery. *J. Climate*. doi:10.1175/JCLI-D-13-00173.1, in press.

© 2013 American Meteorological Society



1 **The Antarctic Atmospheric Energy Budget. Part II: The Effect of**
2 **Ozone Depletion and its Projected Recovery**

3 KAREN L. SMITH * MICHAEL PREVIDI

Lamont-Doherty Earth Observatory, Palisades, NY, USA

4 LORENZO M. POLVANI

*Department of Applied Physics and Mathematics, Department of Earth
and Environmental Sciences, Columbia University, New York, NY, USA*

* *Corresponding author address:* Karen L. Smith, Lamont-Doherty Earth Observatory, 207B Oceanography, 61 Route 9W, P.O. Box 1000, Palisades, NY, 10964.

E-mail: ksmith@ldeo.columbia.edu

ABSTRACT

6 In this study we continue our investigation of the atmospheric energy budget of the Antarctic
7 polar cap (the region poleward of 70°S) using integrations of the Whole Atmosphere Com-
8 munity Climate Model from the year 1960 to 2065. In agreement with observational data,
9 we find that the climatological mean net top-of-atmosphere (TOA) radiative flux is primar-
10 ily balanced by the horizontal energy flux convergence over the polar cap. On interannual
11 timescales, changes in the net TOA radiative flux are also primarily balanced by changes in
12 the energy flux convergence, with the variability in both terms significantly correlated with
13 the Southern Annular Mode (SAM); positive and negative correlations, respectively. On
14 multidecadal timescales, twentieth century stratospheric ozone depletion produces a nega-
15 tive trend in the net TOA radiative flux due to a decrease in the absorbed solar radiation
16 within the atmosphere-surface column. The negative trend in the net TOA radiative flux
17 is balanced by a positive trend in energy flux convergence, primarily in austral summer.
18 This negative (positive) trend in the net TOA radiation (energy flux convergence) occurs
19 despite a positive trend in the SAM, suggesting that the effects of the SAM on the energy
20 budget are overwhelmed by the direct radiative effects of ozone depletion. In the twenty-first
21 century, ozone recovery is expected to reverse the negative trend in the net TOA radiative
22 flux, which would then, again, be balanced by a decrease in the energy flux convergence.
23 Therefore, over the next several decades, ozone recovery will, in all likelihood, mask the
24 effect of GHG warming on the Antarctic energy budget.

1. Introduction

The dominant driver of recent multidecadal change in the Antarctic climate system has been the depletion of stratospheric ozone (see Thompson et al. 2011, for a recent review). The formation of the ozone hole over the South Pole has been associated with a cooling of the stratosphere and much of the Antarctic continent, a warming of the Antarctic peninsula (Steig et al. 2009), a poleward shift of the storm tracks (Polvani et al. 2011b; Son et al. 2010, 2009; Lee and Feldstein 2013), a poleward shift in subtropical precipitation (Kang et al. 2011) and changes in Southern Ocean mixing and ventilation (Sallée et al. 2010; Waugh et al. 2013). The changes in the atmospheric circulation, (i.e. lowered geopotential heights over Antarctica and raised geopotential heights over the Southern mid-latitudes, resulting in strengthened westerlies) are characteristic of the Southern Annular Mode (SAM), the dominant mode of Southern Hemisphere extratropical circulation variability, which has been experiencing a positive trend over the past several decades. Despite the many studies examining the role of ozone depletion in large-scale atmospheric circulation trends, none have examined the implications of ozone depletion for atmospheric energy transport into the Antarctic polar cap.

Compared to the Arctic, the atmospheric energy budget of the Antarctic has received relatively little attention (Cullather and Bosilovich 2012; Genthon and Krinner 1998; Nakamura and Oort 1988). Arctic climate change, including dramatic sea ice loss and surface and mid-tropospheric warming, has motivated numerous studies of the energy budget in this region (Kay et al. 2012; Cullather and Bosilovich 2012; Porter et al. 2010; Serreze et al. 2007; Nakamura and Oort 1988). Although the Antarctic has not experienced comparable polar amplification, the dramatic change in the top-of-atmosphere (TOA) short-wave radiative flux associated with Southern Hemisphere stratospheric ozone depletion has likely had an important influence on the Antarctic energy budget. In addition, the recovery of stratospheric ozone in the future may influence the degree of Southern Hemisphere polar amplification we can expect in the coming decades.

52 In part I, Previdi et al. (in press, hereafter PSP13), we examined the climatological
53 mean and intraseasonal-to-interannual variability of the components of the Antarctic energy
54 budget using reanalysis and satellite data, and found a two-way balance between the net
55 TOA radiative flux and the horizontal energy flux convergence over the polar cap. This
56 two-way balance is reflected in significant and opposite-signed correlations between these
57 terms and the SAM; the net TOA radiative flux is positively correlated with the SAM while
58 the energy flux convergence is negatively correlated with the SAM. In light of the positive
59 trend in the SAM over the past few decades, can one infer from interannual relationships
60 that net TOA flux has been increasing and the energy flux convergence has been decreasing
61 over this time period? This question will be addressed in this study.

62 Although direct observation of the Antarctic climate system over the past several decades
63 has improved, observation of the climate of the high southern latitudes continues to be spa-
64 tially and temporally limited; thus, we need to rely on models and reanalyses to aid us in
65 estimating and interpreting the changes that have occurred. The lack of continuous observa-
66 tional data is a particular hinderance for assessing the multidecadal effect of ozone depletion
67 on the Antarctic energy budget. First, there is no record of the TOA radiative fluxes prior to
68 the formation of the ozone hole. Second, direct satellite measurements of the TOA radiative
69 fluxes in the period since consist of short and discontinuous time series. The longest and
70 most recent record is the Clouds and the Earth's Radiant Energy System (CERES) data set
71 that began in March 2000. However, during the 2000-present time period, ozone levels in
72 the Southern Hemisphere have leveled off due to global regulations on chlorofluorocarbons
73 (CFCs; Scientific Assessment of Ozone Depletion, WMO 2010), making this time period
74 inappropriate for detecting TOA trends due to ozone depletion.

75 The other satellite time series of TOA fluxes is from the Earth Radiation Budget Exper-
76 iment (ERBE) which ran from February 1985 to April 1989. This is a short data set and
77 it is difficult to directly compare it with CERES, given that they are derived from different
78 instruments with their own biases. After some bias correction, Fasullo and Trenberth (2008)

79 show significant differences between climatological ERBE and CERES net TOA short- and
80 long-wave radiative fluxes at high southern latitudes in austral spring, consistent with the
81 effect of ozone depletion (a decrease in both absorbed solar and outgoing long-wave radiation
82 in CERES relative to ERBE; see their Figure 1). It is difficult to attribute these differences
83 to ozone, however, given that differences between the two data sets are significant in many
84 other parts of the globe and at other times of the year (i.e., when ozone depletion would be
85 expected to be unimportant). Furthermore, the CERES data set includes the September 2002
86 stratospheric sudden warming which has likely skewed the springtime mean of the net TOA
87 flux in CERES over Antarctica given that sudden warmings in the Southern Hemisphere
88 are very rare (the September 2002 TOA long-wave flux anomaly averaged from 70-90°S was
89 more than two standard deviations outside the 2001-2010 CERES mean).

90 Reanalyses are extremely useful tools for investigating the climate of the recent past;
91 however, due to the adverse effect of biases in observed ozone on the analysis, reanalysis
92 products do not assimilate time-varying ozone data using analysis schemes that allow ozone
93 to interact with other dynamical fields (Dee et al. 2011). In addition, reanalyses of the high-
94 latitude Southern Hemisphere prior to the satellite era are poorly constrained by observations
95 and must be used with caution (Kistler et al. 2001).

96 In order to circumvent the issues with satellite and reanalysis data, we investigate the ex-
97 tent to which ozone depletion and projected recovery influence the Antarctic energy budget
98 using a fully coupled, state-of-the-art, stratosphere-resolving model with interactive strato-
99 spheric chemistry. In addition to investigating the trends in the Antarctic energy budget
100 in an ensemble of twentieth century model integrations, we also compare two ensembles of
101 twenty-first century integrations, one with and one without ozone recovery. We find that
102 trends in the Antarctic energy budget in the twentieth century are dominated by the effects
103 of ozone depletion, particularly the TOA short-wave radiative flux in spring and summer.
104 In the future, ozone recovery should reverse these trends.

2. Methods

a. Model

We employ the Community Earth System Model Version 1 (CESM1) using the Whole Atmosphere Community Climate Model atmospheric component (CESM1(WACCM); hereafter WACCM), i.e., the stratosphere-resolving, coupled-chemistry version of the National Center for Atmospheric Research (NCAR) Community Atmosphere Model Version 4 (CAM4) (Gent et al. 2011). The land, ocean and sea ice components of WACCM are identical to those in CESM1. In contrast, the WACCM atmospheric component has 66 vertical levels with a model top at 140 km, a horizontal resolution of $1.9^\circ \times 2.5^\circ$, special parameterizations for gravity waves and other upper atmospheric processes and, most importantly, fully-interactive stratospheric chemistry.

The WACCM twentieth century ensemble comprises 3 integrations and extends from the year 1960-2000 (labeled "20C"). These integrations follow the Coupled Model Intercomparison Project Phase 5 (CMIP5) Historical scenario for surface greenhouse gas concentrations (Meinshausen et al. 2011). The Historical scenario also includes prescribed surface concentrations of ozone-depleting substances (ODSs). For further details on the model and the twentieth century integrations the reader is referred to Marsh et al. (2013).

To examine the role of ozone recovery in the twenty-first century we contrast two ensembles of model runs, each comprising 3 integrations, from 2001 to 2065. These model integrations were previously examined in Smith et al. (2012) for Antarctic sea ice. For the first ensemble (labeled "21C"), forcings for the years 2001-2005 are specified following the CMIP5 Historical scenario and forcings for the years 2006-2065 are specified following Representative Concentration Pathway 4.5 (RCP 4.5; Meinshausen et al. 2011). The RCP 4.5 members are initialized from the 3 corresponding Historical integrations described above (Marsh et al. 2013). For the second twenty-first century ensemble (labeled "FixODS"), everything is identical to 21C except for the surface concentrations of ODSs, which are held

131 fixed at year 2000 levels. In other words, we compare two future scenarios in which green-
 132 house gas (GHG) concentrations increase, but one includes ozone recovery (21C) and the
 133 other does not (FixODS). This is shown in Figure 1a, where we plot the ensemble mean
 134 October-November-December (OND) total column ozone, averaged from 70-90°S, for the
 135 twentieth century ensemble and for both twenty-first century ensembles. Southern Hemi-
 136 sphere polar cap ozone decreases dramatically from 1965-2000 (black curve). From 2001
 137 onwards, ozone recovers for the 21C scenario (black curve) but remains constant for the
 138 FixODS scenario (red curve).

139 *b. Energy Budget*

140 We define the energy budget of the atmosphere as,

$$\frac{\partial E}{\partial t} = F_{TOA:NET} + F_{SFC:NET} + F_{WALL} \quad (1)$$

141 where $\frac{\partial E}{\partial t}$ is the vertically integrated atmospheric energy storage, $F_{TOA:NET}$ is the net
 142 top-of-atmosphere (TOA) radiative flux, $F_{SFC:NET}$ is the net surface energy flux (including
 143 radiative, sensible and latent heat fluxes), and F_{WALL} is the vertically integrated horizontal
 144 energy flux convergence. The energy storage term can be written as,

$$\frac{\partial E}{\partial t} = \frac{\partial}{\partial t} \int_0^{p_s} (c_p T + \Phi_s + Lq + k) \frac{dp}{g} \quad (2)$$

145 where g is the gravitational acceleration, p is pressure, p_s is the surface pressure, c_p is
 146 the specific heat of air at constant pressure, T is the absolute temperature, Φ_s is the surface
 147 geopotential, L is the latent heat of vaporization for water, q is the specific humidity and k is
 148 the kinetic energy. The dry static energy (DSE) is the sum of the internal energy, $c_p T$, and
 149 the potential energy, Φ , and the moist static energy (MSE) is the DSE plus the latent energy,
 150 Lq . The terms on the right-hand side of Equation (1), consist of the following components,

$$F_{TOA:NET} = F_{TOA:SW} + F_{TOA:LW} \quad (3)$$

$$F_{SFC:NET} = F_{SFC:SW} + F_{SFC:LW} + F_{SFC:LH+SH} \quad (4)$$

$$F_{WALL} = -\nabla \cdot \int_0^{p_s} (c_p T + \Phi + Lq + k) \vec{v} \frac{dp}{g} \quad (5)$$

151 $F_{TOA:NET}$ (Equation 3) consists of the net TOA short-wave (SW) and long-wave (LW)
 152 radiative fluxes, $F_{TOA:SW}$ and $F_{TOA:LW}$, respectively. These fluxes are alternatively known as
 153 the absorbed solar radiation (ASR) and outgoing long-wave radiation (OLR). Equation (4)
 154 states that $F_{SFC:NET}$ consists of the net surface SW and LW radiative fluxes, $F_{SFC:SW}$ and
 155 $F_{SFC:LW}$, and the net turbulent flux of sensible heat (SH) plus latent heat (LH), $F_{SFC:LH+SH}$.
 156 The default $F_{SFC:LH}$ output by WACCM does not account for the latent heat of snow melt.
 157 This has been included by calculating the latent heat flux associated with snow fall following
 158 the method of Kay et al. (2012). Finally, Equation (5) states that F_{WALL} consists of the
 159 convergence of the vertically integrated horizontal flux of MSE plus kinetic energy, k . A
 160 complete derivation of Equations (1) - (5) is given in Appendix A.

161 TOA and surface fluxes (in Wm^{-2}) are obtained from monthly model output, and $\frac{\partial E}{\partial t}$
 162 was calculated using daily model output following the method of Trenberth (1991). F_{WALL}
 163 is calculated as a residual of the other budget terms (Kay et al. 2012; Porter et al. 2010).
 164 All other model output used in this study, such as sea level pressure (SLP), surface air
 165 temperature (SAT) and cloud properties, is taken from monthly model output. The Antarctic
 166 energy budget terms are defined as area-weighted averages over the polar cap (70-90°S). By
 167 convention, positive energy budget terms indicate that the atmospheric column is gaining
 168 energy while negative terms indicate that the atmospheric column is losing energy.

169 Following PSP13, we focus on how the energy budget is affected by variability in the
 170 SAM. The SAM index is computed using the monthly or seasonal, zonal mean difference
 171 between standardized SLP anomalies at 40°S and 65°S (Marshall 2003).

172 Finally, in Section 3b, when calculating correlations between the Antarctic energy budget
173 components and the SAM, the full 1960-2065 anomaly time series of the data are detrended
174 piece-wise, linearly due to visible changes in magnitudes and/or signs of the trends in the
175 Antarctic resulting from the transition between stratospheric ozone depletion (20C) and
176 future recovery (21C). To do this, we specify two adjacent segments of time series (1960-
177 2000 (20C) and 2001-2065 (21C)) with a shared data point at the year 2000 and remove a
178 continuous, piece-wise linear trend from the full 1960-2065 time series. We have conducted
179 the same analysis for the 20C plus FixODS time series and find that the results are very
180 similar.

181 3. Results

182 a. Climatological Energy Budget

183 In the following two sections, we validate the suitability of using WACCM to investigate
184 trends in the Antarctic energy budget. In this section, we first establish how well WACCM
185 simulates the climatological mean Antarctic energy budget. We compare the model bud-
186 get for the years 2001-2010 with the observational estimate of PSP13. Overall, WACCM
187 simulates the climatological Antarctic energy budget quite well.

188 Table 1 lists the 2001-2010 climatological mean Antarctic energy budget based on the
189 ensemble mean of the WACCM twenty-first century (21C) integrations. The key feature
190 of Table 1 is that the dominant energy balance is between net TOA radiative flux and the
191 horizontal energy flux convergence, $F_{TOA:NET}$ and F_{WALL} (except in December). The net
192 surface flux ($F_{SFC:NET}$) and the energy storage ($\frac{\partial E}{\partial t}$) are generally small. The values for
193 $F_{SFC:NET}$, $\frac{\partial E}{\partial t}$, $F_{TOA:NET}$ and F_{WALL} from Table 1 are also shown in the solid lines in Figure
194 2. The climatology shown in Figure 2 agrees well with the observational estimates of PSP13
195 (dashed lines in Figure 2).

196 The net TOA radiative flux ($F_{TOA:NET}$) is negative throughout the year indicating a

197 net flux of energy from the atmospheric column to space. In winter, the net TOA SW
198 flux, $F_{TOA:SW}$, is essentially zero over the Antarctic polar cap, and the net TOA LW flux,
199 $F_{TOA:LW}$, is balanced by F_{WALL} , while in summer, $F_{TOA:SW}$ and $F_{TOA:LW}$ offset each other
200 significantly, resulting in weaker horizontal energy transport. Consequently, $F_{TOA:NET}$ and
201 F_{WALL} have pronounced seasonal cycles.

202 Although the net surface flux ($F_{SFC:NET}$) tends to be small, it reflects the cancellation
203 of larger magnitude radiative and turbulent flux components. The net surface SW flux
204 ($F_{SFC:SW}$) follows the seasonal cycle of TOA insolation. The net surface LW flux ($F_{SFC:LW}$)
205 varies seasonally in a manner similar to $F_{TOA:LW}$; when surface temperatures are highest
206 in austral summer, $F_{SFC:LW}$ is at a maximum. The turbulent fluxes of moisture and heat,
207 ($F_{SFC:LH+SH}$) are negative throughout most of the year except in December and January.
208 Similar to what we reported in PSP13, we find that the seasonal cycle of $F_{SFC:LH+SH}$ in
209 WACCM is driven by the sensible heat fluxes. The wintertime near-surface temperature
210 inversion over the Antarctic (Figure 3, solid curve) leads to sensible heat fluxes from the
211 atmosphere to the surface. From winter to summer, as surface temperatures increase and
212 the inversion weakens (Figure 3, dashed curve), sensible heat fluxes decrease and latent heat
213 fluxes from the surface to the atmosphere increase slightly resulting in positive $F_{SFC:LH+SH}$
214 fluxes in December and January.

215 As pointed out in PSP13, the different characteristics (e.g., heat capacity, albedo) of the
216 underlying surfaces in the Antarctic and Arctic (the former consisting of perennial land ice
217 and the latter consisting of seasonally ice covered ocean), result in dramatically different
218 net surface energy fluxes. In the Arctic, the seasonal cycles of $F_{SFC:NET}$ and $F_{TOA:NET}$ act
219 to offset one another such that F_{WALL} has relatively little seasonal variation (Porter et al.
220 2010). In the Antarctic, however, the dominant balance throughout the year is between
221 $F_{TOA:NET}$ and F_{WALL} , with $F_{SFC:NET}$ remaining comparatively small in magnitude (Figure
222 2).

223 Comparing the solid (WACCM) and dashed lines (PSP13 estimate) in Figure 2, one can

224 see that WACCM captures the observed magnitude and seasonal variation of the Antarctic
225 energy budget components quite well. In the annual mean, WACCM underestimates the
226 magnitude of $F_{TOA:NET}$ by $\sim 7\%$ and F_{WALL} by $\sim 9\%$. WACCM overestimates the annual
227 mean $F_{SFC:NET}$ by $\sim 33\%$ (due to the small values of $F_{SFC:NET}$). A detailed discussion of the
228 biases in the WACCM Antarctic energy budget is included in Appendix B, but we believe
229 the model adequately serves our aim of studying past and future trends.

230 *b. SAM Variability*

231 In the previous section, we demonstrated that WACCM successfully captures the clima-
232 tological seasonal cycle of the Antarctic energy budget, and is in good agreement with obser-
233 vations. We here turn to the interannual variability. PSP13 showed that the intraseasonal-
234 to-interannual variability of the components of the energy budget is well-correlated with
235 large-scale modes of atmospheric variability, particularly the SAM. In this section, we con-
236 tinue our validation of the simulation of the Antarctic energy budget in WACCM by exam-
237 ining how well it simulates the interannual correlations with the SAM. Since the trend in the
238 large-scale atmospheric circulation in the Southern Hemisphere during the twentieth century
239 period in WACCM is characterized by a positive trend in the SAM (Figures 1b and 1c), it is
240 important to validate the interannual relationships between energy budget components and
241 the SAM in WACCM before we examine the trends.

242 First, we show that the horizontal energy flux convergence (F_{WALL}) and the net TOA
243 radiative flux ($F_{TOA:NET}$) not only balance each other in the climatological mean, but that
244 their detrended anomalies also balance. Figure 4 shows a scatter plot of the annual mean
245 $F_{TOA:NET}$ and F_{WALL} anomalies. In the annual mean, approximately 52% of the variance in
246 F_{WALL} is explained by $F_{TOA:NET}$. Thus, interannual changes in one component are coupled
247 to changes in the other.

248 Second, we find that the observed annual mean correlations between the SAM and the
249 energy budget components are well represented in WACCM. Figure 5 shows scatter plots

250 of the annual mean $F_{TOA:NET}$ (Figure 5a), F_{WALL} (Figure 5b) and $F_{SFC:NET}$ (Figure 5c)
 251 anomalies and the SAM. Note that the scale on the y-axis in panel (c) is different from
 252 panels (a) and (b). In the annual mean, the SAM is positively correlated with $F_{TOA:NET}$
 253 (primarily the LW flux; $R^2 = 0.48$), negatively correlated with F_{WALL} ($R^2 = 0.36$) and
 254 positively correlated with $F_{SFC:NET}$ ($R^2 = 0.22$). These regressions are all significant at the
 255 95% level and qualitatively agree with the observational equivalents discussed in PSP13.

256 Third, we compare the seasonal correlations between the energy budget components and
 257 the SAM with PSP13 (Table 2). WACCM captures the sign and approximate magnitude of
 258 the correlations between $F_{TOA:SW}$, $F_{TOA:LW}$ and $F_{TOA:NET}$ and the SAM in both JJA and
 259 DJF (compare with Table 2 of PSP13). We note that the negative $F_{TOA:SW}$ -SAM correlation
 260 in DJF in WACCM arises primarily from the clear-sky component of $F_{TOA:SW}$, and this is
 261 due in part to the negative correlation between total column ozone and the SAM during this
 262 season.

263 Broadly, the positive annual mean correlations between $F_{TOA:NET}$ and the SAM reflect a
 264 decrease in outgoing LW radiation during the positive phase of the SAM when the Antarctic
 265 continent is anomalously cold. In DJF, the positive correlation between $F_{TOA:LW}$ and the
 266 SAM is offset by a negative correlation with $F_{TOA:SW}$ (i.e., a decrease in absorbed solar
 267 radiation when the SAM is positive) which results in a weaker $F_{TOA:NET}$ -SAM correlation
 268 in DJF.

269 We also note several differences between the seasonal correlations in WACCM and in
 270 the observations (see Table 2 of PSP13). Several of the differences are in the surface flux
 271 correlations which are the least constrained flux estimates in the observational energy budget
 272 of PSP13 (Berrisford et al. 2011). In the remainder of this section, we discuss the details of
 273 these differences.

274 In both DJF and JJA, we find positive correlations with $F_{SFC:SH+LH}$ (primarily $F_{SFC:SH}$)
 275 and the SAM. PSP13 also find positive correlations in both seasons although the JJA cor-
 276 relation is not significant in the observations.

277 The SAM correlation with $F_{SFC:LW}$ in JJA is also positive in WACCM but is insignificant
278 in the observations. The sign of this correlation requires some clarification. There is a signif-
279 icant negative correlation between the *upward* $F_{SFC:LW}$ and the SAM in JJA in WACCM,
280 which agrees with the negative correlation between surface temperature and the SAM (not
281 shown). However, there is also a negative correlation between the *downward* $F_{SFC:LW}$ in
282 JJA. The net effect is that the cooling of the atmospheric column during the positive phase
283 of the SAM leads to a decrease in downward $F_{SFC:LW}$ that exceeds the decrease in upward
284 $F_{SFC:LW}$. The cooling of the atmospheric column also explains the positive correlation in
285 WACCM between $F_{SFC:SH+LH}$ and the SAM in JJA due to a decrease in downward SH flux
286 (Table 2). In the annual mean (Figure 5c), the main contribution to the net surface flux is
287 the net surface LW flux, $F_{SFC:LW}$, and the explanation for the sign of the correlation is the
288 same as the JJA correlation.

289 Finally, we find a negative correlation between F_{WALL} and the SAM in DJF and JJA
290 in WACCM, again not present in the observations. This correlation implies that when the
291 SAM is in its positive phase, i.e. the westerly jet is poleward shifted, the horizontal energy
292 flux into Antarctica decreases. With respect to the two-way balance between F_{WALL} and
293 $F_{TOA:NET}$, these negative correlations in DJF and JJA agree with the positive $F_{TOA:NET}$ -
294 SAM correlations in these seasons. They also agree with the sign of the annual mean
295 correlation shown in Figure 5b.

296 Overall, the annual mean relationships between the energy budget components and the
297 SAM are well-represented in WACCM, and Figure 5 suggests that the relationships between
298 the energy budget terms and the SAM in the annual mean are most representative of the
299 relationships for JJA (Table 2). There are several seasonal differences in the SAM correla-
300 tions between WACCM and the observations, and we note that these differences may be due
301 in part to the short-time series of the observational record (Table 2 of PSP13 used data for
302 the 2001-2010 time period only).

303 Having confirmed that our WACCM simulations generally capture both the mean and the

304 variability of the Antarctic energy budget, in the next subsection we examine the recent past
305 and projected future trends in the Antarctic energy budget. We will show that accounting
306 for the direct effect of stratospheric ozone depletion and recovery on the radiative fluxes is
307 crucial for interpreting the energy budget trends.

308 *c. Multidecadal Trends: Ozone Depletion and Recovery*

309 As one can see from the black curves in Figures 1b and 1c, the summertime and annual
310 mean WACCM trends in the SAM during the twentieth century period are positive. The
311 largest positive trends occur in austral summer and are associated with springtime strato-
312 spheric ozone depletion, but weaker positive trends are also evident in winter and spring
313 (not shown). Based on the above correlations between the SAM and the net TOA radiative
314 flux ($F_{TOA:NET}$) and the relationship between $F_{TOA:NET}$ and the horizontal energy flux con-
315 vergence, F_{WALL} , one might expect to find a contemporaneous positive trend in the annual
316 mean $F_{TOA:NET}$ and negative trend in F_{WALL} over this time period. Likewise, as the trend
317 in the SAM is projected to change considerably in the future (21C), the trends in the energy
318 budget components may be expected to change accordingly. However, this is not what we
319 find in the WACCM simulations. The depletion and recovery of stratospheric ozone over
320 the South Pole has a dramatic effect on $F_{TOA:SW}$, and it completely overwhelms the SAM
321 trends.

322 Figure 6a shows the time series of October-November-December (OND) averaged net
323 TOA SW flux ($F_{TOA:SW}$) in WACCM. OND is the season when stratospheric ozone depletion
324 occurs over the South Pole. $F_{TOA:SW}$ decreases dramatically over the twentieth century time
325 period when ozone depletion occurs (compare with Figure 1a). The decrease in net $F_{TOA:SW}$
326 is due to the fact that less downward SW radiation is absorbed in the atmospheric column by
327 stratospheric ozone and therefore more SW radiation reaches the clouds and the surface and
328 is reflected back to space. Additionally, less of the reflected upward SW is absorbed in the
329 stratosphere by the ozone layer. The result is an increase in upward SW and, thus, a decrease

330 in net SW at the TOA ($F_{TOA:SW}$). The largest contribution to the twentieth century trend
331 shown in Figure 6a results from the clear-sky component of $F_{TOA:SW}$ (not shown); however,
332 the trend is slightly amplified (a $\sim 1 \text{ Wm}^{-2}$ decrease from 1960-2000) due to an increase
333 in total cloud fraction during this time period, shown in Figure 6c. The increase in total
334 cloud fraction is associated with the poleward shift of the storm tracks. Note that the TOA
335 SW trends are not associated with the positive trend in the SAM in OND as the detrended
336 $F_{TOA:SW}$ -SAM relationship in OND is not statistically significant (not shown). Overall, the
337 interannual relationships between the energy budget components and the SAM in OND are
338 very similar to those in JJA (see Table 2).

339 In the twenty-first century, $F_{TOA:SW}$ increases as ozone recovers in the 21C scenario, but
340 remains relatively constant for the FixODS scenario (Figure 6a). Total cloud fraction de-
341 creases slightly in the 21C scenario, complementing the effect of ozone recovery on $F_{TOA:SW}$,
342 but changes little with FixODS (Figure 6c). The only difference between our two twenty-first
343 century simulations is the prescribed surface concentrations of ODSs, and thus the differ-
344 ence in the twenty-first century energy budget trends can be directly and unambiguously
345 attributed to the differences in stratospheric ozone.

346 Figure 6b shows the time series of net TOA LW flux ($F_{TOA:LW}$) in OND in WACCM.
347 $F_{TOA:LW}$ is also altered by the changes in stratospheric ozone. During the twentieth century
348 period, when ozone depletion occurs, $F_{TOA:LW}$ increases due to cooling of the stratosphere
349 and the surface/troposphere (in accordance with the positive trend in the SAM). Greenhouse
350 gas (GHG) forcing also contributes to the cooling of the stratosphere. The increase in
351 $F_{TOA:LW}$ is about half the magnitude of the decrease in $F_{TOA:SW}$ over the 1960-2000 time
352 period, resulting in a pronounced negative $F_{TOA:NET}$ trend in OND (Figure 7a). As ozone
353 recovers (21C), $F_{TOA:LW}$ decreases, illustrating the combined warming of the stratosphere
354 (due to ozone recovery) and the surface/troposphere (due to increases in GHG). For the
355 FixODS scenario, the surface/troposphere warms but the stratosphere continues to cool
356 causing a weaker decrease in $F_{TOA:LW}$.

357 The key role of ozone depletion and recovery is brought to light by considering the
 358 seasonal cycle of the trends in the twentieth and twenty-first century periods. Figure 7a
 359 shows the monthly twentieth century trends for $F_{TOA:NET}$ in WACCM. Negative trends are
 360 statistically significant in austral spring, as one might expect. During the twentieth century
 361 period, $F_{TOA:NET}$ decreases due to the decrease in $F_{TOA:SW}$. Note that the detrended,
 362 interannual $F_{TOA:NET}$ -SAM correlation in OND is positive and statistically significant (not
 363 shown), suggesting that a positive trend in the SAM in OND cannot explain the negative
 364 trends in $F_{TOA:NET}$ in Figure 7a.

365 In the twenty-first century, for the 21C scenario, the increase in $F_{TOA:SW}$ results in a
 366 positive trend in $F_{TOA:NET}$ in austral spring, while for the FixODS scenario, the decrease
 367 in $F_{TOA:LW}$ leads to a weak negative trend in $F_{TOA:NET}$ in spring. This is shown in the
 368 differences (21C - FixODS) between the $F_{TOA:NET}$ trends in the twenty-first century (Figure
 369 7c). The differences are positive and statistically significant at the 95% level in OND. The
 370 statistically significant $F_{TOA:NET}$ trend differences in April and May reflect two processes;
 371 first, ozone recovery from an approximate 15% loss occurs in these months which leads to
 372 increased absorbed SW radiation and second, significant sea ice loss near the continent in the
 373 FixODS scenario relative to the 21C scenario leads to enhanced warming near the Antarctic
 374 coast (see Figure 3b of Smith et al. (2012)) and increased outgoing LW radiation. Studies
 375 have shown that the climate effects of independently prescribed GHG forcing and ozone
 376 recovery in GCMs are approximately additive (Polvani et al. 2011a; McLandress et al. 2011)
 377 thus, the effect of GHG forcing on $F_{TOA:NET}$ roughly subtracts out in Figure 7c.

378 For both the twentieth and twenty-first century periods, the trends in OND $F_{TOA:NET}$
 379 are evident in liked-signed trends in the energy tendency, $\frac{\partial E}{\partial t}$, for the same season (not
 380 shown). Notably, these trends in $F_{TOA:NET}$ coincide with opposite signed trends in the SAM,
 381 particularly in December. In other words, the positive interannual correlation between the
 382 SAM and $F_{TOA:NET}$ described in Section 3b is nowhere to be seen in the trends. Again, this
 383 shows that stratospheric ozone is the controlling factor, and the SAM does not give useful

384 information about long-term trends (contrast Figures 1b and 7a and 7c).

385 Having examined $F_{TOA:NET}$, we now turn to the horizontal energy flux convergence,
386 F_{WALL} . Figure 7b shows the monthly twentieth century trends for F_{WALL} in WACCM.
387 Austral summer is the season which experiences the largest positive trends in F_{WALL} , par-
388 ticularly in January when the trend is statistically significant at the 95% level. There is also
389 a positive trend in the SAM in summer during the twentieth century period (Figure 1b).
390 Although an investigation of the dynamical mechanisms that drive the trends in F_{WALL} is
391 beyond the scope of this paper, it is clear that the trends in F_{WALL} act to compensate for
392 the trends in $F_{TOA:NET}$ one to two months earlier.

393 In the twenty-first century, the trend in F_{WALL} reverses sign in summer as ozone recovers
394 and is weakly positive for the FixODS scenario (not shown). The differences between the
395 F_{WALL} trends in the two twenty-first century scenarios (21C - FixODS) are shown in Figure
396 7d and are statistically significant at the 95% level in January. For both the twentieth and
397 twenty-first century scenarios, the F_{WALL} trends are reflected in like-signed trends in $\frac{\partial E}{\partial t}$
398 during the summer season (not shown).

399 As for the net surface flux ($F_{SFC:NET}$), there are no significant trends in the 20C, 21C or
400 FixODS simulations in any month (not shown). This further demonstrates that the two-way
401 balance between $F_{TOA:NET}$ and F_{WALL} in the Antarctic region found in the climatological
402 mean and on intraseasonal-to-interannual timescales also carries over to the multidecadal
403 timescale changes considered here. This balance, characteristic of the Antarctic and very
404 much unlike the Arctic, appears to hold on all time scales.

405 Finally, the annual mean trends in the Antarctic atmospheric energy budget are shown in
406 Figure 8. The annual mean time series of $F_{TOA:NET}$ (Figure 8a) shows a negative trend during
407 the decades of ozone depletion. In the twenty-first century as ozone recovers (21C), there
408 is very little trend in $F_{TOA:NET}$ due to opposite-signed trends in $F_{TOA:LW}$ and $F_{TOA:SW}$,
409 with the SW changes being confined to the OND season and the LW changes occurring
410 throughout the year. The effect of future GHG forcing alone on the annual mean $F_{TOA:NET}$

411 is clearly seen in the FixODS scenario, indicating a weak but significant negative trend due
412 to increased outgoing LW radiation.

413 Figure 8b shows the annual mean time series of F_{WALL} . During the twentieth century
414 period, the negative trend in $F_{TOA:NET}$ (Figure 8a) is balanced by a positive trend in F_{WALL} .
415 For the 21C scenario, Figure 8b depicts a relatively flat trend, consistent with the weak trend
416 in $F_{TOA:NET}$ for the same scenario. For the FixODS scenario, which represents the effect of
417 GHG forcing alone, a positive F_{WALL} trend balances the negative trend in $F_{TOA:NET}$. Thus,
418 Figure 8 suggests that projected ozone recovery mitigates the increase in horizontal energy
419 flux into the Antarctic polar cap associated with GHG warming.

420 4. Summary and Conclusions

421 In this paper, we have extended our examination of the Antarctic atmospheric energy
422 budget using an ensemble of integrations of the CESM1(WACCM) climate model. We find
423 that WACCM reproduces the climatological energy budget reasonably well relative to the
424 observational estimate presented in PSP13. In addition, we have shown that WACCM is
425 able to capture the observed interannual relationships between the energy budget terms and
426 the SAM. A large fraction of the interannual variability in the energy budget terms can be
427 explained by the SAM, particularly in austral winter. In the annual mean, the net TOA
428 radiative flux, $F_{TOA:NET}$, and the horizontal energy flux convergence, F_{WALL} , are positively
429 and negatively correlated with the SAM, respectively.

430 From an energy balance perspective, the opposite-signed interannual correlations reflect
431 the fact that, seasonally and in the annual mean, energy balance over the Antarctic polar
432 cap is primarily satisfied through compensating changes in F_{WALL} and $F_{TOA:NET}$. From
433 a dynamical perspective, however, the negative correlation between F_{WALL} and the SAM
434 might seem counterintuitive. During the positive phase of the SAM the baroclinic zone is
435 shifted poleward and one would naively guess this would result in larger energy flux into the

436 polar cap by synoptic eddies; yet the opposite is found in both WACCM and the reanalysis
437 (PSP13). Weaker energy flux during the positive phase of the SAM suggests that synoptic
438 eddies may become less efficient at transporting energy with a poleward-displaced baroclinic
439 zone (Carleton and Whalley 1988). This dynamical interpretation is complicated, however,
440 by the fact that the twentieth century summertime trend in F_{WALL} is *positive* when the
441 SAM is trending positive and the westerly jet is shifting poleward. Our investigation of the
442 nature of the relationship between F_{WALL} and the SAM is ongoing.

443 On multidecadal timescales, the effects of ozone depletion and projected recovery domi-
444 nate the trends in the Antarctic energy budget from 1960-2065. During the twentieth century
445 period from 1960-2000, ozone depletion results in an annual mean decrease in $F_{TOA:NET}$ due
446 to the decrease in $F_{TOA:SW}$. This is balanced by an increase in F_{WALL} . In the twenty-first
447 century as ozone recovers, the opposite-signed trends in the net TOA SW and LW fluxes
448 ($F_{TOA:SW}$ and $F_{TOA:LW}$) result in little trend in $F_{TOA:NET}$ and consequently, F_{WALL} . An
449 alternative twenty-first century scenario in which GHG warming occurs in the absence of
450 ozone recovery shows a continued increase in F_{WALL} in the future. Thus, the future posi-
451 tive trend in energy flux convergence into the Antarctic polar cap due to GHG warming is
452 mitigated by ozone recovery.

453 This study highlights the fact that the annual mean interannual correlations between
454 the SAM and $F_{TOA:NET}$ and F_{WALL} do not help to explain the multidecadal trends in these
455 fluxes. Smith et al. (2012) arrived at a similar conclusion with respect to the SAM and
456 Antarctic sea ice trends. Although the SAM is a good predictor of interannual variations in
457 Antarctic climate, we emphasize that the SAM may not be a good predictor of multidecadal
458 trends in the Antarctic climate system and we caution against using the SAM as a means of
459 explaining trends.

460 The role of energy flux convergence in future Antarctic polar amplification is currently
461 unknown. As GCMs do not yet include dynamic Antarctic ice sheet and ice shelf components,
462 it is unclear how increases in well-mixed GHGs and ozone recovery will affect the Antarctic

463 surface energy balance in the future and how changes in the surface energy balance will
464 be compensated for by changes in other components of the Antarctic atmospheric energy
465 budget. Our WACCM simulations show no statistically significant trend in $F_{SFC:NET}$ in
466 either the 21C or FixODS twenty-first century scenarios. Despite current model limitations,
467 our work suggests that the effect of ozone recovery in the future may mask the effect of GHG
468 warming on the Antarctic energy budget for several decades.

469 *Acknowledgments.*

470 The authors would like to gratefully acknowledge the NSF Antarctic Sciences Program,
471 ANT-09-44063. The CESM Project is supported by the National Science Foundation (NSF)
472 and the Office of Science (BER) of the U.S. Department of Energy. All model integrations
473 were performed at the National Center for Atmospheric Research (NCAR), which is spon-
474 sored by the U.S. NSF. We would like to thank Dan Marsh, Mike Mills, and Doug Kinnison
475 at NCAR for their assistance with the model integrations.

Vertically-Integrated Atmospheric Energy Budget Derivation

Some of the steps needed to obtain Equations (1) - (5) are mentioned in the literature, e.g. Trenberth and Solomon (1994) and Trenberth (1997). However, we were unable to find a complete and coherent derivation of these equations from first principles. Hence, for the sake of completeness, we include it here with enough detail to make the derivation easily understandable. We start with the thermodynamic equation,

$$c_p \left[\frac{\partial T}{\partial t} + \vec{v} \cdot \nabla T + \omega \left(\frac{\partial T}{\partial p} - \kappa \frac{T}{p} \right) \right] = Q \quad (\text{A1})$$

where T is temperature, \vec{v} is the horizontal wind vector, ω is the vertical wind component, p is pressure, c_p is the isobaric specific heat capacity, κ is the ratio of the specific gas constant, R , to c_p , and Q is the diabatic heating. The kinetic energy equation is obtained by taking the dot product of the horizontal momentum equations with \vec{v} ,

$$\frac{\partial k}{\partial t} + \nabla \cdot k\vec{v} + \frac{\partial k\omega}{\partial p} = -\vec{v} \cdot \nabla \Phi + \vec{v} \cdot \vec{F} \quad (\text{A2})$$

where k is the kinetic energy, Φ is the geopotential and \vec{F} is friction. Neglecting frictional dissipation and using the ideal gas law, the hydrostatic equation and the continuity equation, the sum of Equations (A1) and (A2) can be written as,

$$\frac{\partial(c_p T + k)}{\partial t} + \nabla \cdot (c_p T + \Phi + k)\vec{v} + \frac{\partial(c_p T + \Phi + k)\omega}{\partial p} = Q \quad (\text{A3})$$

493 Next, we add the moisture equation to Equation (A3) to obtain,

$$\frac{\partial(c_p T + k + Lq)}{\partial t} + \nabla \cdot (c_p T + \Phi + k + Lq)\vec{v} + \frac{\partial(c_p T + \Phi + k + Lq)\omega}{\partial p} = Q + L(e - c) \quad (\text{A4})$$

494 where q is the specific humidity, L is the latent heat of vaporization for water, e is the
 495 rate of evaporation and c is the rate of condensation within the atmosphere per unit mass.
 496 Now, we vertically integrate Equation (A4) and use the Leibniz Rule to take $\frac{\partial}{\partial t}$ and $\nabla \cdot$
 497 outside of the integrals. The terms on the left-hand side of Equation (A4) become,

$$\int_0^{p_s} \frac{\partial(c_p T + k + Lq)}{\partial t} \frac{dp}{g} = \frac{\partial}{\partial t} \int_0^{p_s} (c_p T + k + Lq) \frac{dp}{g} - \frac{1}{g} (c_p T + k + Lq)|_{p_s} \frac{\partial p_s}{\partial t} \quad (\text{A5})$$

$$\int_0^{p_s} \nabla \cdot (c_p T + \Phi + k + Lq)\vec{v} \frac{dp}{g} = \nabla \cdot \int_0^{p_s} (c_p T + \Phi + k + Lq)\vec{v} \frac{dp}{g} - \frac{1}{g} (c_p T + k + Lq)\vec{v}|_{p_s} \cdot \nabla p_s \quad (\text{A6})$$

$$\int_0^{p_s} \frac{\partial(c_p T + \Phi + k + Lq)}{\partial p} \frac{dp}{g} = \frac{1}{g} (c_p T + \Phi + k + Lq)\omega|_{p_s} \quad (\text{A7})$$

498 where subscript s indicates the surface value. In order to reduce these terms to the form
 499 outlined in Section 2b, we use the definition of ω evaluated at the surface,

$$\omega_s = \frac{\partial p_s}{\partial t} + \vec{v}_s \cdot \nabla p_s \quad (\text{A8})$$

500 Substituting ω_s in Equation (A7) for Equation (A8), and substituting Equations (A5)-
 501 (A7) in Equation (A4), many of the terms cancel and we end up with

$$\begin{aligned} \frac{\partial}{\partial t} \int_0^{p_s} (c_p T + k + Lq) \frac{dp}{g} + \nabla \cdot \int_0^{p_s} (c_p T + \Phi + k + Lq)\vec{v} \frac{dp}{g} - \frac{1}{g} \Phi_s \vec{v}_s \cdot \nabla p_s + \frac{1}{g} \Phi_s \omega_s \\ = \int_0^{p_s} (Q + L(e - c)) \frac{dp}{g} \quad (\text{A9}) \end{aligned}$$

502 Substituting Equation (A8) into Equation (A9), and re-arranging the partial derivatives,
 503 we get

$$\begin{aligned} \frac{\partial}{\partial t} \int_0^{p_s} (c_p T + k + Lq) \frac{dp}{g} + \nabla \cdot \int_0^{p_s} (c_p T + \Phi + k + Lq) \vec{v} \frac{dp}{g} + \frac{1}{g} \frac{\partial p_s \Phi_s}{\partial t} \\ = \int_0^{p_s} (Q + L(e - c)) \frac{dp}{g} \end{aligned} \quad (\text{A10})$$

504 Finally, taking the $\frac{\partial p_s \Phi_s}{\partial t}$ inside the integral gives,

$$\begin{aligned} \frac{\partial}{\partial t} \int_0^{p_s} (c_p T + k + Lq + \Phi_s) \frac{dp}{g} + \nabla \cdot \int_0^{p_s} (c_p T + \Phi + k + Lq) \vec{v} \frac{dp}{g} \\ = \int_0^{p_s} (Q + L(e - c)) \frac{dp}{g} \end{aligned} \quad (\text{A11})$$

505 The left-hand side of Equation (A11) is now in the form shown in Section 2b. The
 506 right-hand side of Equation (A11) can be re-written as,

$$\int_0^{p_s} (Q + L(e - c)) \frac{dp}{g} = F_{TOA:NET} + F_{SFC:RAD} + F_{SFC:SH} + LP + L(E - P) \quad (\text{A12})$$

507 where $F_{TOA:NET}$ is the net radiative flux at the top-of-the-atmosphere, $F_{SFC:RAD}$ is the
 508 net radiative flux at the surface, $F_{SFC:SH}$ is the surface sensible heat flux and P and E are
 509 the precipitation and the surface evaporation rates. LE is equivalent to the surface latent
 510 heat flux, $F_{SFC:LH}$. Thus, the complete energy budget equation as outlined in Section 2b is
 511 as follows,

$$\begin{aligned} \frac{\partial}{\partial t} \int_0^{p_s} (c_p T + k + Lq + \Phi_s) \frac{dp}{g} + \nabla \cdot \int_0^{p_s} (c_p T + \Phi + k + Lq) \vec{v} \frac{dp}{g} \\ = F_{TOA:NET} + F_{SFC:NET} \end{aligned} \quad (\text{A13})$$

512 where $F_{TOA:NET}$ and $F_{SFC:NET}$ are as defined in Equations (3) and (4) in Section 2b.

Antarctic Atmospheric Energy Budget Biases in WACCM

Data

We use several observational data products to examine the biases in the Antarctic atmospheric energy budget in WACCM. We use the CERES satellite data of TOA radiative fluxes from 2001-2010. Monthly CERES TOA fluxes from the EBAF (Energy Balanced and Filled) dataset are obtained on a $1^\circ \times 1^\circ$ grid from the NASA Langley Research Center Atmospheric Science Data Center. To produce the EBAF data, CERES TOA short-wave (SW) and long-wave (LW) fluxes are adjusted such that the global mean net TOA flux (averaged over several years) is equal to the estimated present-day change in heat storage in the Earth system (Loeb et al. 2009). This procedure thus eliminates the unrealistically large global mean TOA flux that exists in the unadjusted CERES data (Trenberth et al. 2009). We also use the associated computed CERES surface radiative flux product for 2001-2010 (Kratz et al. 2010).

To assess the model-simulated cloud cover, we use satellite derived total cloud fraction and cloud mean water path from the International Satellite Cloud Climatology Project (ISCCP), which provides complete spatial coverage of the Antarctic polar cap (Rossow and Schiffer 1999). Climatological monthly mean ISCCP fields based on data from July 1983 to December 2009 are obtained on a $2.5^\circ \times 2.5^\circ$ grid from the NASA Goddard Institute for Space Studies.

Column ozone in WACCM is compared to the AC&C/SPARC ozone database for 2001-2009. This database was created as a joint effort between the Chemistry-Climate Modeling

537 Validation (CCMVal) Activity of the World Meteorological Organization’s Stratospheric Pro-
538 cesses and their Role in Climate (SPARC) project and the Atmospheric Chemistry and Cli-
539 mate (AC&C) Initiative, for use as a forcing for CMIP5 general circulation models (GCMs)
540 that do not include interactive ozone chemistry (Cionni et al. 2011). For 2001-2009, the
541 AC&C/SPARC stratospheric ozone database is generated in a manner similar to Randel
542 and Wu (2007).

543 Lastly, we compare WACCM surface air temperature (SAT) for 2001-2010 to observations
544 from 18 Antarctic weather stations (see Figure 1 in Previdi et al. in press). These observations
545 were made available as part of the Reference Antarctic Data for Environmental Research
546 (READER) project (Turner and Colwell 2004).

547 *Model Biases*

548 Figure 9a shows the TOA biases in WACCM relative to CERES for the 2001-2010 period.
549 The blue curve shows the $F_{TOA:NET}$ bias relative to CERES, which is positive throughout the
550 year except in December. The positive bias in $F_{TOA:NET}$ arises primarily due to the positive
551 bias in the $F_{TOA:LW}$ component, while the negative $F_{TOA:NET}$ bias in December arises from
552 the negative bias in $F_{TOA:SW}$ (solid red curve).

553 In general, there is no consensus on the sign of $F_{TOA:LW}$ biases in the Antarctic across
554 reanalyses and GCMs (Trenberth and Fasullo 2010). The positive bias in WACCM is mainly
555 due to the cold SAT bias in WACCM over the Antarctic region. Figure 9b (black curve)
556 shows the WACCM SAT relative to Antarctic station data from READER (see Figure 1 of
557 PSP13 for station locations). The seasonal cycle of the WACCM $F_{TOA:LW}$ bias (Figure 9a)
558 generally agrees with the SAT bias.

559 In addition to the surface air temperature bias, WACCM displays a negative stratospheric
560 ozone bias (Figure 9d; polar cap averaged (70-90°S) and column integrated between 500 and
561 1 hPa) relative to the AC&C/SPARC ozone database for the time period 2001-2009. The
562 ozone bias may also be contributing to the positive $F_{TOA:LW}$ bias in WACCM, particularly

563 in austral spring. A negative bias in ozone cools the stratosphere due to a decrease in
564 absorption of SW radiation. Indeed, the lower stratosphere in WACCM is known to be
565 biased cold (Marsh et al. 2013). The AC&C/SPARC ozone database is constructed using
566 satellite and ozonesonde data and may itself be biased somewhat high in the Antarctic
567 relative to other observationally based ozone climatologies (Hassler et al. 2012).

568 The SW biases in WACCM (Figure 9a) are not typical of reanalyses and GCMs (Tren-
569 berth and Fasullo 2010). Trenberth and Fasullo (2010) show that reanalyses and GCMs
570 typically overestimate $F_{TOA:SW}$ at high southern latitudes. In contrast, WACCM underes-
571 timates $F_{TOA:SW}$, particularly in austral spring and summer. CCSM3 was also shown to
572 underestimate $F_{TOA:SW}$ over the Antarctic polar cap (Briegleb and Bromwich 1998). In fall,
573 a negative WACCM bias in upward $F_{TOA:SW}$ is partially offset by a positive bias in downward
574 solar flux in WACCM relative to CERES (dotted red curve, Figure 9a). In spring, a fraction
575 of the negative WACCM bias in $F_{TOA:SW}$ can be attributed to too little downward solar
576 flux at the top of the atmosphere. The remainder of the negative bias is explained by the
577 fact that WACCM is reflecting more SW radiation from the surface and atmosphere back to
578 space compared to CERES (dashed red curve, Figure 9a). We attribute this to WACCM's
579 positive bias in surface albedo (Figure 9b) and negative bias in stratospheric ozone (Figure
580 9d).

581 Figure 9b shows WACCM's polar cap averaged surface albedo bias relative to CERES
582 (red curve). During polar night, we are unable to get a reliable estimate of the surface albedo
583 from CERES SW fluxes. The WACCM bias in surface albedo results in a positive bias in
584 upward $F_{SFC:SW}$ in the model (Figure 9b, blue curve). To verify that the $F_{TOA:SW}$ bias is
585 not directly related to biases in the simulated cloud fields, we plot the WACCM biases in
586 total cloud amount, CLDTOT, and cloud mean water path, CLDMWP, relative to ISCCP
587 in Figure 9c. It is important to note that there are challenges when comparing model-
588 simulated cloud data with satellite-derived data, particularly in polar regions where satellite
589 products contain significant biases (Bromwich et al. 2012). For example, ISCCP, which is

590 based on passive visible-infrared (VIS-IR) retrievals, is missing CLDMWP information at
591 high latitudes from February through September due to very low insolation during these
592 months.

593 Unlike the CMIP3 models and CCSM3, which typically overestimate cloud amount over
594 the Antarctic polar cap throughout the year (Bromwich et al. 2012; Briegleb and Bromwich
595 1998), WACCM tends to underestimate cloud amount in late spring, summer and fall and
596 overestimate in winter and early spring. When the $F_{TOA:SW}$ bias is largest in late austral
597 spring, WACCM has negative biases in both CLDTOT and CLDMWP (Figure 9c). This
598 indicates that the negative bias in $F_{TOA:SW}$ is likely not due to increased SW reflection back
599 to space due to a greater amount of brighter clouds in WACCM. In fact, the negative biases
600 in cloud properties in WACCM act to amplify the effect of the surface albedo bias on the
601 $F_{TOA:SW}$ bias. A detailed analysis of the cloud properties in WACCM is beyond the scope
602 of this study.

603 The negative bias in stratospheric ozone may also contribute to the negative $F_{TOA:SW}$
604 bias in WACCM. A negative bias in ozone indicates that less SW radiation is absorbed by
605 ozone and is, therefore, available to be reflected back to space by the surface, clouds and
606 atmosphere.

REFERENCES

- 609 Berrisford, P., P. Kållberg, S. Kobayashi, D. Dee, S. Uppala, A. J. Simmons, P. Poli, and
610 H. Sato, 2011: Atmospheric conservation properties in ERAInterim. *Quarterly Journal of*
611 *the Royal Meteorological Society*, **137 (659)**, 1381–1399, doi:10.1002/qj.864.
- 612 Briegleb, B. and D. Bromwich, 1998: Polar Radiation Budgets of the NCAR CCM3. *Journal*
613 *of Climate*, **11**, 1246–1269.
- 614 Bromwich, D., J. Nicolas, and K. Hines, 2012: Tropospheric clouds in Antarctica. *Reviews*
615 *of Geophysics*, **50**, 1–40, doi:10.1029/2011RG000363.1.INTRODUCTION.
- 616 Carleton, A. and D. Whalley, 1988: Eddy Transport of Sensible Heat and the Life His-
617 tory of Synoptic Systems : A Statistical Analysis for the Southern Hemisphere Winter.
618 *Meteorology and Atmospheric Physics*, **38**, 140–152.
- 619 Cionni, I., et al., 2011: Ozone database in support of CMIP5 simulations: results and
620 corresponding radiative forcing. *Atmospheric Chemistry and Physics*, **11 (21)**, 11 267–
621 11 292, doi:10.5194/acp-11-11267-2011.
- 622 Cullather, R. I. and M. G. Bosilovich, 2012: The Energy Budget of the Polar Atmosphere
623 in MERRA. *Journal of Climate*, **25 (1)**, 5–24, doi:10.1175/2011JCLI4138.1.
- 624 Dee, D. P., et al., 2011: The ERA-Interim reanalysis: configuration and performance
625 of the data assimilation system. *Quarterly Journal of the Royal Meteorological Society*,
626 **137 (656)**, 553–597, doi:10.1002/qj.828.
- 627 Fasullo, J. T. and K. E. Trenberth, 2008: The Annual Cycle of the Energy Budget. Part II:
628 Meridional Structures and Poleward Transports. *Journal of Climate*, **21 (10)**, 2313–2325,
629 doi:10.1175/2007JCLI1936.1.

- 630 Gent, P. R., et al., 2011: The Community Climate System Model Version 4. *Journal of*
631 *Climate*, **24 (19)**, 4973–4991, doi:10.1175/2011JCLI4083.1.
- 632 Genthon, C. and G. Krinner, 1998: Convergence and disposal of energy and moisture on
633 the Antarctic polar cap from ECMWF reanalyses and forecasts. *Journal of climate*, **11**,
634 1703–1716.
- 635 Hassler, B., P. J. Young, R. W. Portmann, G. E. Bodeker, J. S. Daniel, K. H. Rosenlof, and
636 S. Solomon, 2012: Comparison of three vertically resolved ozone data bases: climatology,
637 trends and radiative forcings. *Atmospheric Chemistry and Physics Discussions*, **12 (10)**,
638 26 561–26 605, doi:10.5194/acpd-12-26561-2012.
- 639 Kang, S. M., L. M. Polvani, J. C. Fyfe, and M. Sigmond, 2011: Impact of polar ozone
640 depletion on subtropical precipitation. *Science*, **332 (6032)**, 951–4, doi:10.1126/science.
641 1202131.
- 642 Kay, J. E., M. M. Holland, C. M. Bitz, E. Blanchard-Wrigglesworth, A. Gettelman, A. Con-
643 ley, and D. Bailey, 2012: The Influence of Local Feedbacks and Northward Heat Transport
644 on the Equilibrium Arctic Climate Response to Increased Greenhouse Gas Forcing. *Journal*
645 *of Climate*, **25 (16)**, 5433–5450, doi:10.1175/JCLI-D-11-00622.1.
- 646 Kistler, R., E. Kalnay, and W. Collins, 2001: The NCEP-NCAR 50-year reanalysis: Monthly
647 means CD-ROM and documentation. *Bulletin of the American Meteorological Society*,
648 **82 (February 2001)**, 247–268.
- 649 Kratz, D. P., S. K. Gupta, A. C. Wilber, and V. E. Sothcott, 2010: Validation of the
650 CERES Edition 2B Surface-Only Flux Algorithms. *Journal of Applied Meteorology and*
651 *Climatology*, **49 (1)**, 164–180, doi:10.1175/2009JAMC2246.1.
- 652 Lee, S. and S. B. Feldstein, 2013: Detecting Ozone- and Greenhouse Gas-Driven Wind Trends
653 with Observational Data. *Science*, **339 (6119)**, 563–567, doi:10.1126/science.1225154.

654 Loeb, N. G., B. a. Wielicki, D. R. Doelling, G. L. Smith, D. F. Keyes, S. Kato, N. Manalo-
655 Smith, and T. Wong, 2009: Toward Optimal Closure of the Earth's Top-of-Atmosphere
656 Radiation Budget. *Journal of Climate*, **22** (3), 748–766, doi:10.1175/2008JCLI2637.1.

657 Marsh, D. R., M. J. Mills, D. E. Kinnison, J.-f. Lamarque, N. Calvo, and L. M. Polvani, 2013:
658 Climate change from 1850 to 2005 simulated in CESM1(WACCM). *Journal of Climate*,
659 **1**, 1305091150556 003, doi:10.1175/JCLI-D-12-00558.1.

660 Marshall, G., 2003: Trends in the Southern Annular Mode from observations and reanalyses.
661 *Journal of Climate*, **16** (1999), 4134–4143.

662 McLandress, C., T. G. Shepherd, J. F. Scinocca, D. a. Plummer, M. Sigmond, A. I. Jonsson,
663 and M. C. Reader, 2011: Separating the Dynamical Effects of Climate Change and Ozone
664 Depletion. Part II: Southern Hemisphere Troposphere. *Journal of Climate*, **24** (6), 1850–
665 1868, doi:10.1175/2010JCLI3958.1.

666 Meinshausen, M., et al., 2011: The RCP greenhouse gas concentrations and their extensions
667 from 1765 to 2300. *Climatic Change*, **109** (1-2), 213–241, doi:10.1007/s10584-011-0156-z.

668 Nakamura, N. and A. Oort, 1988: Atmospheric heat budgets of the polar regions. *Journal*
669 *of Geophysical Research*, **93** (D8), 9510–9524.

670 Polvani, L. M., M. Previdi, and C. Deser, 2011a: Large cancellation, due to ozone recovery, of
671 future Southern Hemisphere atmospheric circulation trends. *Geophysical Research Letters*,
672 **38** (4), 1–6, doi:10.1029/2011GL046712.

673 Polvani, L. M., D. W. Waugh, G. J. P. Correa, and S.-W. Son, 2011b: Stratospheric
674 Ozone Depletion: The Main Driver of Twentieth-Century Atmospheric Circulation
675 Changes in the Southern Hemisphere. *Journal of Climate*, **24** (3), 795–812, doi:10.1175/
676 2010JCLI3772.1.

677 Porter, D. F., J. J. Cassano, M. C. Serreze, and D. N. Kindig, 2010: New estimates of the
678 large-scale Arctic atmospheric energy budget. *Journal of Geophysical Research*, **115** (D8),
679 1–16, doi:10.1029/2009JD012653.

680 Previdi, M., K. L. Smith, and L. M. Polvani, in press: The Antarctic Atmospheric En-
681 ergy Budget. Part I: Climatology and Intraseasonal-to-Interannual Variability. *Journal of*
682 *Climate*.

683 Randel, W. J. and F. Wu, 2007: A stratospheric ozone profile data set for 19792005: Vari-
684 ability, trends, and comparisons with column ozone data. *Journal of Geophysical Research*,
685 **112** (D6), D06 313, doi:10.1029/2006JD007339.

686 Rossow, W. B. and R. a. Schiffer, 1999: Advances in Understanding Clouds from IS-
687 CCP. *Bulletin of the American Meteorological Society*, **80** (11), 2261–2287, doi:10.1175/
688 1520-0477(1999)080<2261:AIUCFI>2.0.CO;2.

689 Sallée, J. B., K. G. Speer, and S. R. Rintoul, 2010: Zonally asymmetric response of the
690 Southern Ocean mixed-layer depth to the Southern Annular Mode. *Nature Geoscience*,
691 **3** (4), 273–279, doi:10.1038/ngeo812.

692 Serreze, M. C., A. P. Barrett, A. G. Slater, M. Steele, J. Zhang, and K. E. Trenberth, 2007:
693 The large-scale energy budget of the Arctic. *Journal of Geophysical Research*, **112** (D11),
694 1–17, doi:10.1029/2006JD008230.

695 Smith, K. L., L. M. Polvani, and D. R. Marsh, 2012: Mitigation of 21st century Antarctic sea
696 ice loss by stratospheric ozone recovery. *Geophysical Research Letters*, **39** (20), L20 701,
697 doi:10.1029/2012GL053325.

698 Son, S.-W., N. F. Tandon, L. M. Polvani, and D. W. Waugh, 2009: Ozone hole and Southern
699 Hemisphere climate change. *Geophysical Research Letters*, **36** (15), 1–5, doi:10.1029/
700 2009GL038671.

701 Son, S.-W., et al., 2010: Impact of stratospheric ozone on Southern Hemisphere circulation
702 change: A multimodel assessment. *Journal of Geophysical Research*, **115**, 1–18, doi:10.
703 1029/2010JD014271.

704 Steig, E. J., D. P. Schneider, S. D. Rutherford, M. E. Mann, J. C. Comiso, and D. T.
705 Shindell, 2009: Warming of the Antarctic ice-sheet surface since the 1957 International
706 Geophysical Year. *Nature*, **457 (7228)**, 459–62, doi:10.1038/nature07669.

707 Thompson, D. W. J., S. Solomon, P. J. Kushner, M. H. England, K. M. Grise, and D. J.
708 Karoly, 2011: Signatures of the Antarctic ozone hole in Southern Hemisphere surface
709 climate change. *Nature Geoscience*, **4 (11)**, 741–749, doi:10.1038/ngeo1296.

710 Trenberth, K., 1997: The definition of El Nino. *Bulletin of the American Meteorological*
711 *Society*, **78 (August)**, 2771–2777.

712 Trenberth, K. and A. Solomon, 1994: The global heat balance: Heat transports in the
713 atmosphere and ocean. *Climate Dynamics*, **10**, 107–134.

714 Trenberth, K. E., 1991: Climate diagnostics from global analyses- Conservation of mass in
715 ECMWF analyses. *Journal of Climate*, **4**, 707–722.

716 Trenberth, K. E. and J. T. Fasullo, 2010: Simulation of Present-Day and Twenty-First-
717 Century Energy Budgets of the Southern Oceans. *Journal of Climate*, **23 (2)**, 440–454,
718 doi:10.1175/2009JCLI3152.1.

719 Trenberth, K. E., J. T. Fasullo, and J. Kiehl, 2009: Earth’s Global Energy Budget. *Bulletin*
720 *of the American Meteorological Society*, **90 (3)**, 311–323, doi:10.1175/2008BAMS2634.1.

721 Turner, J. and S. Colwell, 2004: The SCAR READER project: toward a high-quality
722 database of mean Antarctic meteorological observations. *Journal of Climate*, **17**, 2890–
723 2898.

724 Waugh, D. W., F. Primeau, T. Devries, and M. Holzer, 2013: Recent changes in the venti-
725 lation of the southern oceans. *Science*, **339** (6119), 568–70, doi:10.1126/science.1225411.

726 WMO, 2010: Scientific Assessment of Ozone Depletion: 2010; Global Ozone Research and
727 Monitoring Project Report No. 52. Tech. rep., 516 pp.

728 List of Tables

- 729 1 Monthly and annual mean WACCM climatological mean Antarctic energy
730 budget components for 2001-2010. Values are based on the ensemble mean of
731 the WACCM twenty-first century (21C) integrations. All values are in Wm^{-2}
732 with positive values indicating energy gain by the atmospheric column. 34
- 733 2 December-January-February (DJF) and June-July-August (JJA) correlations
734 between piece-wise, linearly detrended Antarctic energy budget components
735 and the SAM for 1960-2065 (20C + 21C). Bold font indicates correlations
736 that are statistically significant at the 95% level. 35

	$\frac{\partial E}{\partial t}$	$F_{TOA:SW}$	$F_{TOA:LW}$	$F_{TOA:NET}$	$F_{SFC:SW}$	$F_{SFC:LW}$	$F_{SFC:LH+SH}$	$F_{SFC:NET}$	F_{WALL}
Jan	7	164	-194	-30	-81	59	6	-16	51
Feb	-8	106	-182	-76	-50	51	-1	0	66
Mar	-19	41	-163	-122	-17	42	-11	14	87
Apr	-15	7	-148	-141	-2	36	-21	13	110
May	-13	1	-140	-139	0	35	-23	12	113
Jun	-7	0	-131	-131	0	35	-23	12	110
Jul	-6	0	-125	-125	0	35	-23	12	104
Aug	-1	2	-125	-123	-1	36	-23	12	107
Sept	6	18	-131	-113	-7	38	-21	10	106
Oct	12	60	-144	-84	-27	45	-13	5	89
Nov	20	121	-165	-44	-58	55	-3	-6	68
Dec	23	168	-186	-18	-83	61	5	-17	56
Annual	0	57	-153	-95	-27	44	-13	4	89

TABLE 1. Monthly and annual mean WACCM climatological mean Antarctic energy budget components for 2001-2010. Values are based on the ensemble mean of the WACCM twenty-first century (21C) integrations. All values are in Wm^{-2} with positive values indicating energy gain by the atmospheric column.

	$\frac{\partial E}{\partial t}$	$F_{TOA:SW}$	$F_{TOA:LW}$	$F_{TOA:NET}$	$F_{SFC:SW}$	$F_{SFC:LW}$	$F_{SFC:LH+SH}$	$F_{SFC:NET}$	F_{WALL}
DJF	-0.006	-0.34	0.55	0.20	0.14	0.11	0.24	0.56	-0.26
JJA	-0.10	0.12	0.59	0.59	-0.15	0.39	0.28	0.46	-0.49

TABLE 2. December-January-February (DJF) and June-July-August (JJA) correlations between piece-wise, linearly detrended Antarctic energy budget components and the SAM for 1960-2065 (20C + 21C). Bold font indicates correlations that are statistically significant at the 95% level.

737 List of Figures

- 738 1 WACCM time series of (a) polar cap averaged (70-90°S) October-November-
739 December (OND) total column ozone, (b) December-January-February SAM,
740 and (c) annual mean SAM for the years 1960-2065. Black curve indicates the
741 20C + 21C scenarios and red curve indicates the FixODS scenario (ensemble
742 means). Individual ensemble members are shown in thin gray and pink curves. 38
- 743 2 2001-2010 climatological atmospheric energy budget components averaged
744 over the polar cap (70-90°S). The black, blue, green and red solid curves
745 show the energy storage, $\frac{\partial E}{\partial t}$, net top-of-atmosphere radiative flux, $F_{TOA:NET}$,
746 the net surface radiative and turbulent fluxes, $F_{SFC:NET}$, and the horizontal
747 energy flux convergence, F_{WALL} . The dashed curves show the corresponding
748 energy budget terms for the observational data for the same time period from
749 Table 1 of PSP13. 39
- 750 3 Vertical profile of polar cap averaged (70-90°S) temperature for June-July-
751 August (JJA; solid curve) and December-January-February (DJF; dashed
752 curve). Data points below the Antarctic surface are not included. 40
- 753 4 Scatter plot of WACCM annual mean, piece-wise, linearly detrended polar
754 cap averaged (70-90°S) $F_{TOA:NET}$ and F_{WALL} anomalies for 1960-2065 (20C
755 + 21C). Solid black line indicates the least-squares linear fit to the data. 41
- 756 5 Scatter plots of the WACCM annual mean, piece-wise, linearly detrended
757 SAM and the polar cap averaged (70-90°S) (a) $F_{TOA:NET}$, (b) F_{WALL} , and (c)
758 $F_{SFC:NET}$ anomalies for 1960-2065 (20C + 21C). Solid black lines indicate the
759 least-squares linear fit to the data. Note that the y-axis in panel (c) differs
760 from panels (a) and (b). 42

761	6	WACCM time series of polar cap averaged October-November-December (OND)	
762		(a) $F_{TOA:SW}$, (b) $F_{TOA:LW}$ and (c) total cloud fraction. Black curve indi-	
763		cates the 20C + 21C scenarios and red curve indicates the FixODS scenario.	
764		Least-squares linear fits to the 20C, 21C and FixODS are shown. Individual	
765		ensemble members are shown in thin gray and pink curves.	43
766	7	Bar plots of monthly twentieth century (20C) trends for polar cap averaged	
767		(70-90°S) (a) $F_{TOA:NET}$ and (b) F_{WALL} in $\text{Wm}^{-2}\text{dec}^{-1}$. (c) and (d) as in	
768		(a) and (b) but showing the difference in twenty-first century trends (21C -	
769		FixODS). Statistical significance is shown by the crosses (95%) and double	
770		crosses (99%).	44
771	8	As in Figure 6 but for annual mean (a) $F_{TOA:NET}$ and (b) F_{WALL} .	45
772	9	(a) 2001-2010 WACCM biases in top-of-atmosphere radiative fluxes (i.e., WACCM	
773		minus CERES). The solid blue, black and red curves show the $F_{TOA:NET}$ bias,	
774		$F_{TOA:LW}$ bias and $F_{TOA:SW}$ bias relative to CERES. The dotted and dashed	
775		red curves show the downward and upward components of the $F_{TOA:SW}$ bias	
776		relative to CERES. (b) 2001-2010 WACCM biases in surface air temperature	
777		(SAT) relative to Antarctic station data (black curve), polarcap averaged (70-	
778		90°S) surface albedo relative to CERES (red curve) and polar cap averaged	
779		(70-90°S) upward $F_{SFC:SW}$ relative to CERES (blue curve). To calculate the	
780		SAT bias, the nearest WACCM grid point to each READER station was	
781		selected and the SAT bias was averaged over all selected grid points. (c)	
782		1983-2009 WACCM biases in total cloud fraction, CLDTOT (black curve),	
783		and total cloud mean water path, CLDMWP (red curve), relative to ISCCP.	
784		(d) 2001-2009 WACCM bias in column ozone (polar cap averaged and ver-	
785		tically integrated from 500 to 1 hPa) relative to the AC&C/SPARC ozone	
786		database.	46

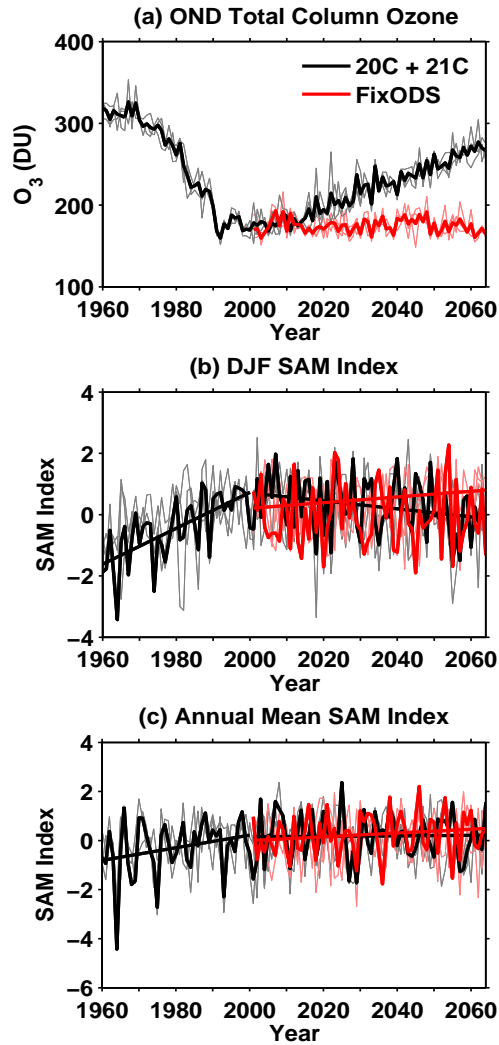


FIG. 1. WACCM time series of (a) polar cap averaged (70-90°S) October-November-December (OND) total column ozone, (b) December-January-February SAM, and (c) annual mean SAM for the years 1960-2065. Black curve indicates the 20C + 21C scenarios and red curve indicates the FixODS scenario (ensemble means). Individual ensemble members are shown in thin gray and pink curves.

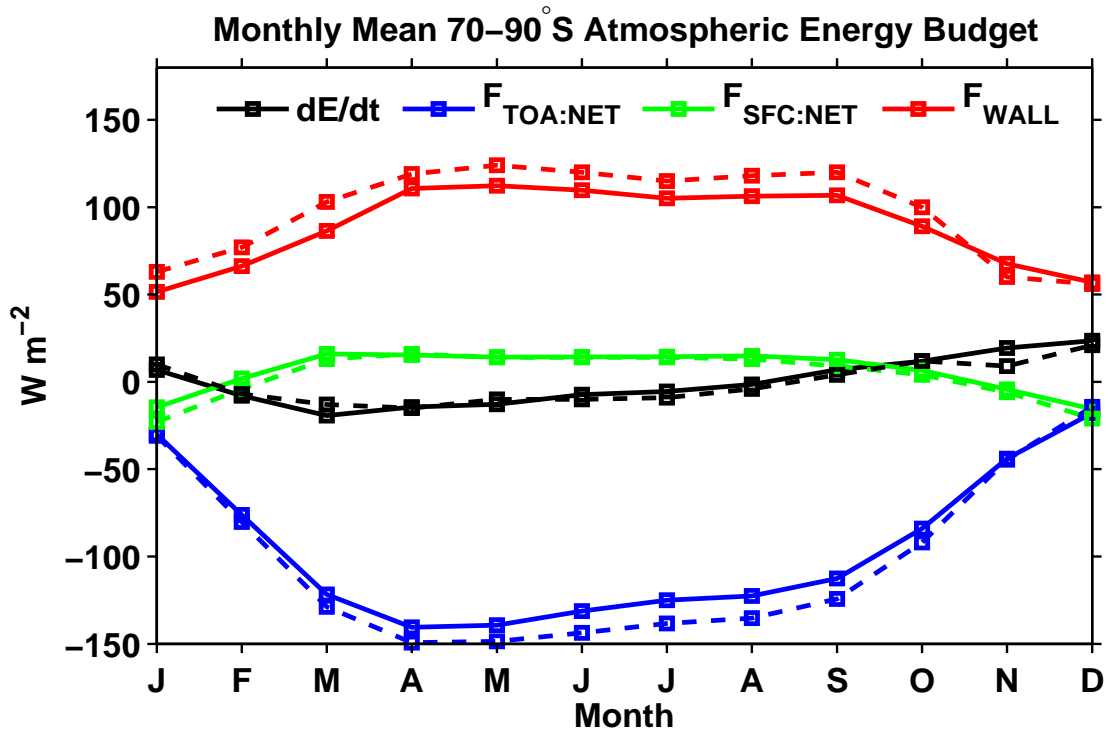


FIG. 2. 2001-2010 climatological atmospheric energy budget components averaged over the polar cap (70-90°S). The black, blue, green and red solid curves show the energy storage, $\frac{\partial E}{\partial t}$, net top-of-atmosphere radiative flux, $F_{TOA:NET}$, the net surface radiative and turbulent fluxes, $F_{SFC:NET}$, and the horizontal energy flux convergence, F_{WALL} . The dashed curves show the corresponding energy budget terms for the observational data for the same time period from Table 1 of PSP13.

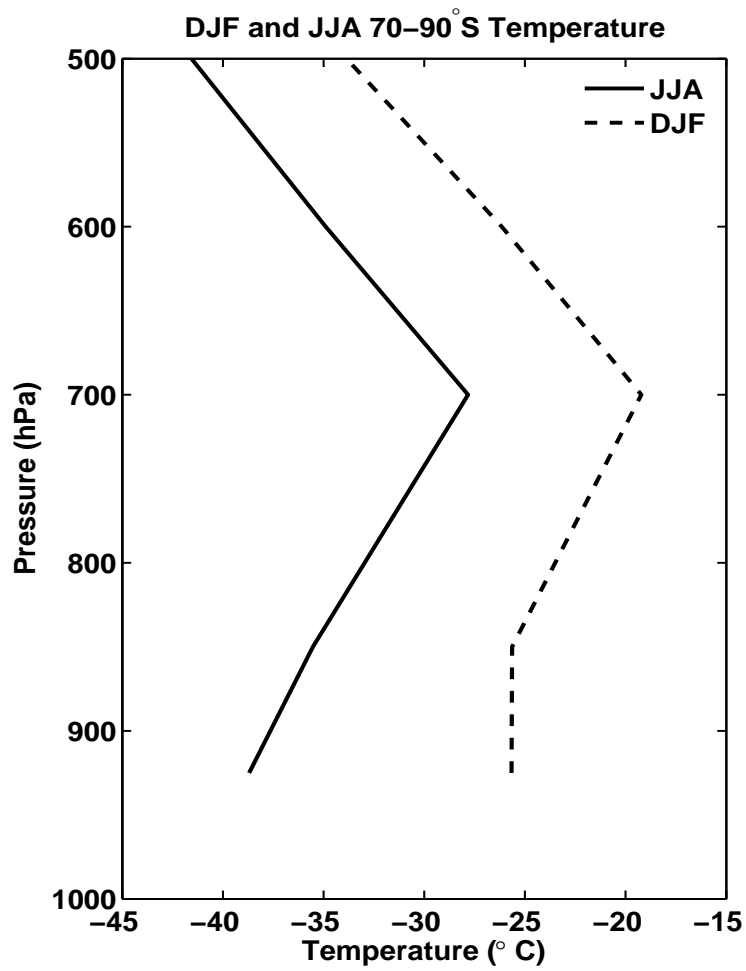


FIG. 3. Vertical profile of polar cap averaged (70-90°S) temperature for June-July-August (JJA; solid curve) and December-January-February (DJF; dashed curve). Data points below the Antarctic surface are not included.

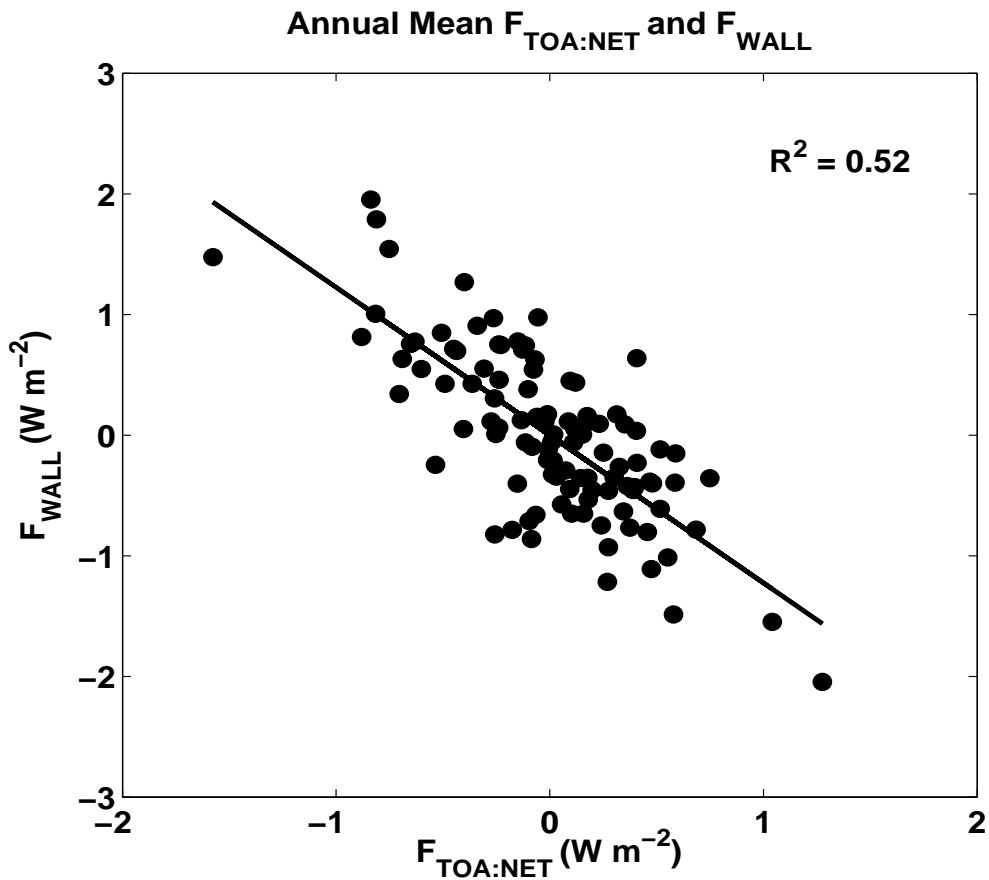


FIG. 4. Scatter plot of WACCM annual mean, piece-wise, linearly detrended polar cap averaged (70-90°S) $F_{TOA:NET}$ and F_{WALL} anomalies for 1960-2065 (20C + 21C). Solid black line indicates the least-squares linear fit to the data.

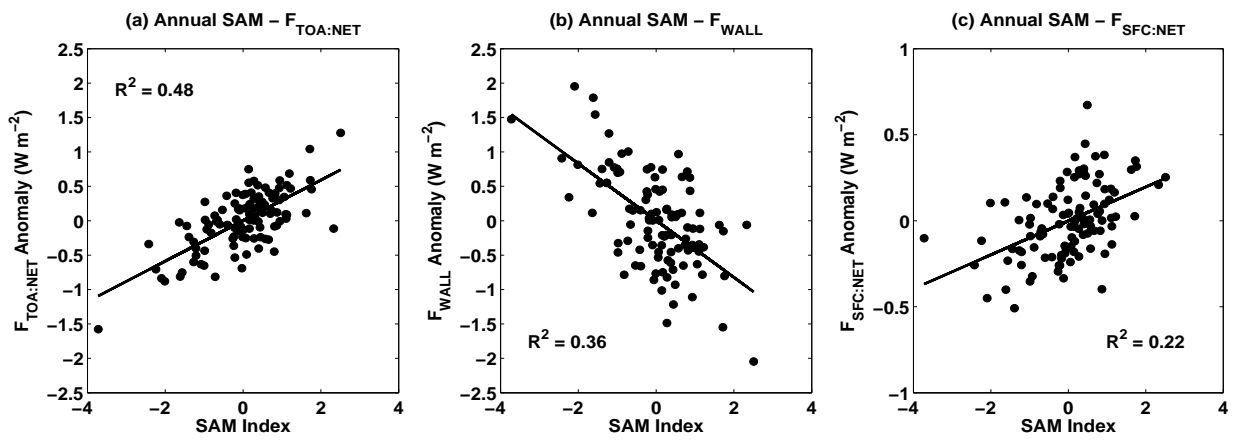


FIG. 5. Scatter plots of the WACCM annual mean, piece-wise, linearly detrended SAM and the polar cap averaged ($70-90^{\circ}S$) (a) $F_{TOA:NET}$, (b) F_{WALL} , and (c) $F_{SFC:NET}$ anomalies for 1960-2065 (20C + 21C). Solid black lines indicate the least-squares linear fit to the data. Note that the y-axis in panel (c) differs from panels (a) and (b).

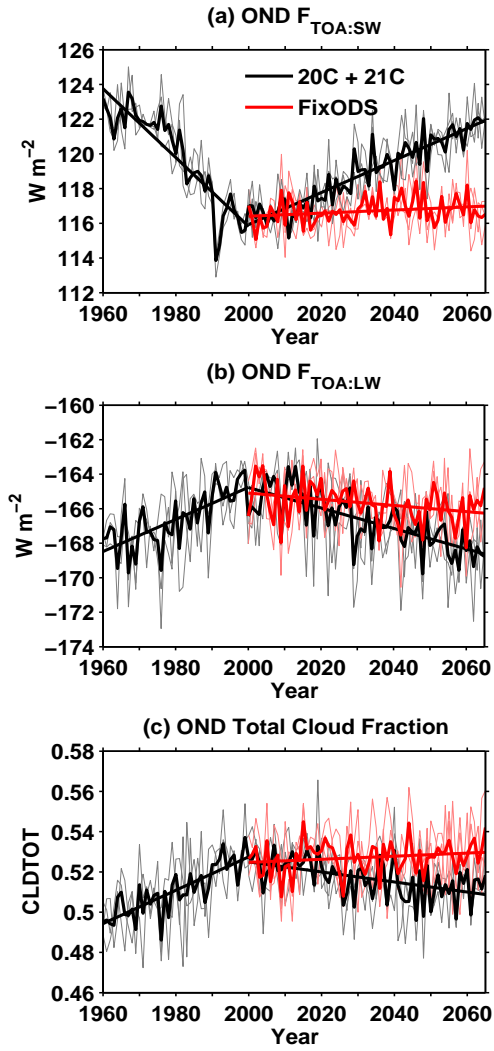


FIG. 6. WACCM time series of polar cap averaged October-November-December (OND) (a) $F_{TOA:SW}$, (b) $F_{TOA:LW}$ and (c) total cloud fraction. Black curve indicates the 20C + 21C scenarios and red curve indicates the FixODS scenario. Least-squares linear fits to the 20C, 21C and FixODS are shown. Individual ensemble members are shown in thin gray and pink curves.

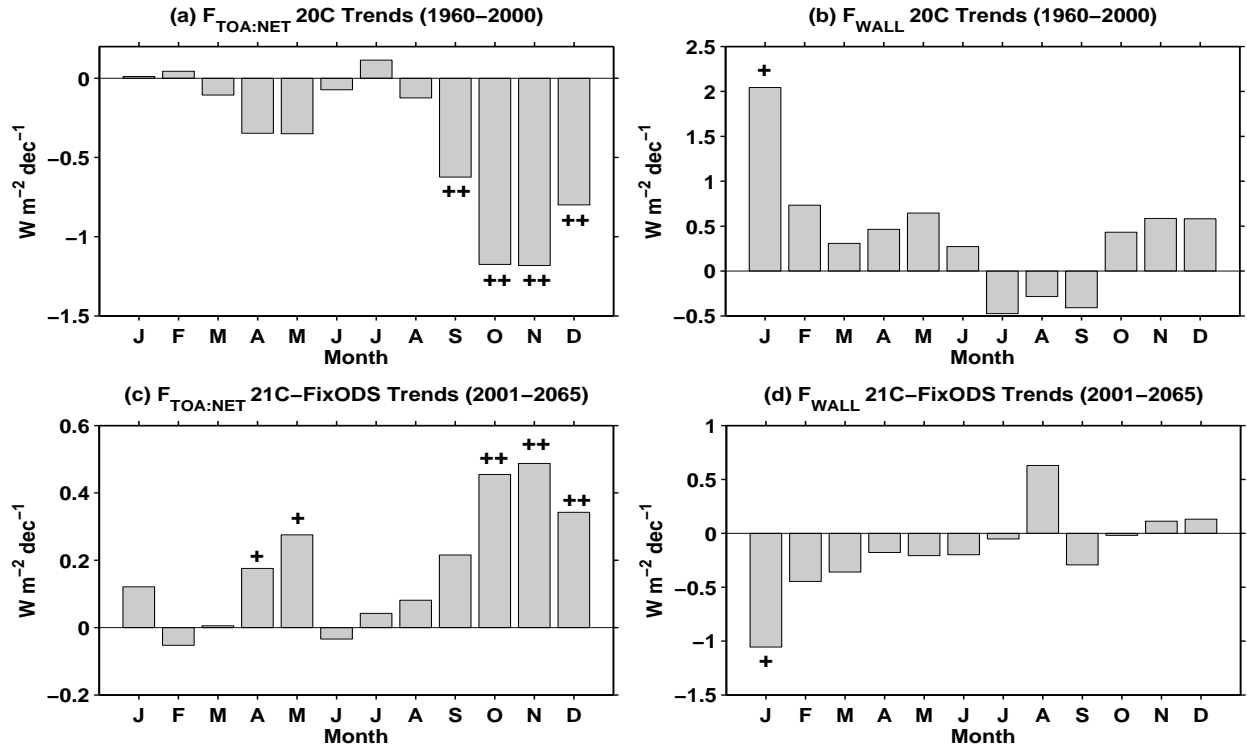


FIG. 7. Bar plots of monthly twentieth century (20C) trends for polar cap averaged (70-90°S) (a) $F_{TOA:NET}$ and (b) F_{WALL} in $Wm^{-2}dec^{-1}$. (c) and (d) as in (a) and (b) but showing the difference in twenty-first century trends (21C - FixODS). Statistical significance is shown by the crosses (95%) and double crosses (99%).

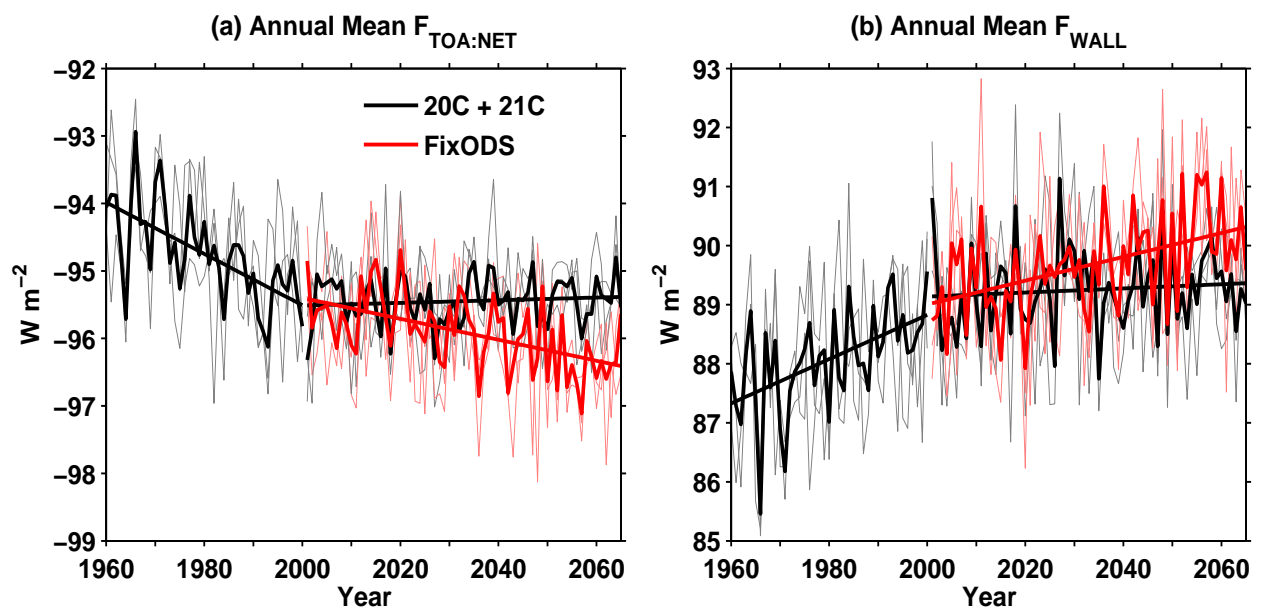


FIG. 8. As in Figure 6 but for annual mean (a) $F_{TOA:NET}$ and (b) F_{WALL} .

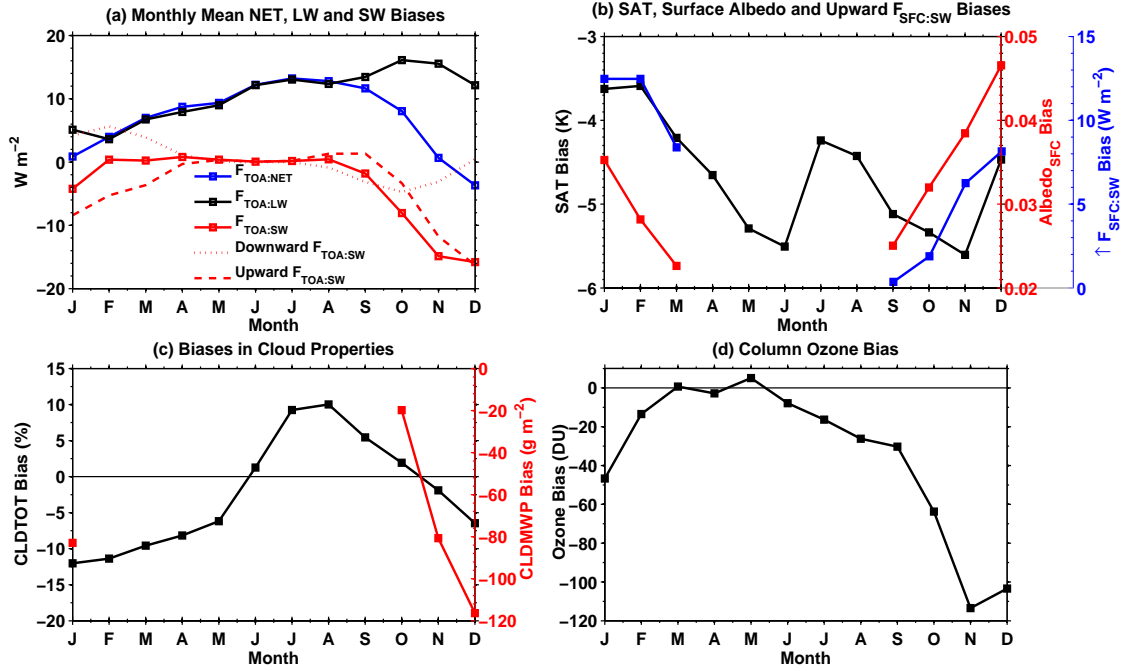


FIG. 9. (a) 2001-2010 WACCM biases in top-of-atmosphere radiative fluxes (i.e., WACCM minus CERES). The solid blue, black and red curves show the $F_{TOA:NET}$ bias, $F_{TOA:LW}$ bias and $F_{TOA:SW}$ bias relative to CERES. The dotted and dashed red curves show the downward and upward components of the $F_{TOA:SW}$ bias relative to CERES. (b) 2001-2010 WACCM biases in surface air temperature (SAT) relative to Antarctic station data (black curve), polarcap averaged (70-90°S) surface albedo relative to CERES (red curve) and polar cap averaged (70-90°S) upward $F_{SFC:SW}$ relative to CERES (blue curve). To calculate the SAT bias, the nearest WACCM grid point to each READER station was selected and the SAT bias was averaged over all selected grid points. (c) 1983-2009 WACCM biases in total cloud fraction, CLDTOT (black curve), and total cloud mean water path, CLDMWP (red curve), relative to ISCCP. (d) 2001-2009 WACCM bias in column ozone (polar cap averaged and vertically integrated from 500 to 1 hPa) relative to the AC&C/SPARC ozone database.